RSC Advances

ROYAL SOCIETY OF CHEMISTRY

www.rsc.org/advances

ARTICLE TYPE www. rsc.org/xxxxxx | XXXXXXXX

Inertia- and deformation-driven migration of a soft particle in confined shear and Poiseuille flow

Yeng-Long Chen[*a,b,c]

Received Xth XXXXXXXXXX 20XX, Accepted Xth XXXXXXXXX 20XX
First published on the web Xth XXXXXXXXXX 200X
DOI: 10.1039/b000000x

Cross-stream migration of dilute soft particle suspensions under simple shear flow and Poiseuille flow between two parallel plates is investigated with lattice Boltzmann-immersed boundary method. Competition between particle elastic contraction, fluid shear forces, and fluid inertial stress drives particle migration to a particular steady state position. With small shear rate, the migration velocity of hard and soft particles is captured by first order analysis of the Navier-Stokes equation. With moderate shear flow, the qualitative dependence of the migration velocity and particle position on shear rate for both hard and soft particles deviate from the predictions. In moderate Reynolds number (Re) shear flow, the observed hard sphere migration velocity has weaker dependence on Re than predicted and also higher order dependence on the particle distance from the channel center. For soft spheres, a migration-free zone is observed near the center at moderate Re and Weissenberg number (Wi). In Poiseuille flow, the soft particle migrates away from the wall to an off-center position dependent on the particle deformation and inertia, in contrast to hard sphere migration where the steady state position is independence of shear rate.

1 Introduction

The non-Newtonian rheological properties of soft colloidal suspensions are mainly caused by the evolving particle structure under flow, such as aggregation, breakup, and particle deformation. The properties of these suspensions strongly depend on the coupling between inter- and intra-particle structure and fluid forces. For example, the strong shear-thinning of blood is due to red cell rouleaux break-up, red cell deformation and lateral migration away from the vessel walls. [1] Similarly, shear-thinning and -thickening of polymer and colloidal suspensions strongly depend on the evolution of aggregation and molecular structural changes under flow shear force. [2,3] Understanding the structural evolution of these suspensions is critical for understanding the micro-circulation and other flow-related phenomena. [4–11]

The complex dynamics of soft particle flow is known to depend on the particle elasticity, shape, concentration and interparticle repulsion/attraction. In applications such as microcapsule drug delivery and microfluidic droplet reactors, controlling particle shape and dynamics is critical for ensuring delivery to the intended target via microflow[12]. In blood micro-circulation, it is known that blood viscosity decreases when the flow shear rate increases in micro-capillaries.[1,13] This 'shear-thinning' effect depends strongly on the diameter of the blood vessel relative to the cell size and the flow shear rate. In addition, the dynamics of the spherical soft white blood cells (WBC) are known to be coupled to the flow of the biconcave discoid elastic red blood cells (RBC) and vice versa [4,6,11,14–19]. To disentangle the complex interactions between different components in blood flow, models for deformable particles (DP) and fluid flow are needed to understand how DP-fluid, DP-vessel and DP-DP hydrodynamic coupling affect the fluid and particle motion.

Cross-stream lateral migration of soft deformable particles can be attributed to the asymmetric hydrodynamic field produced by an elastic particle near a wall, and the unbalanced fluid stress about the particle surface. For a deformable particle in a suspension, the competition between the particle shape-restoring elasticity, the elastic relaxation time τ_{relax}, and the flow shear force, is one factor that determines the migration velocity. The deformation-driven migration force can thus be characterized by the capillary number $Ca = \dot{\gamma}\eta R/G$, where η is the fluid viscosity, R is the particle radius, G is the surface elastic modulus, and $\dot{\gamma}$ is the flow shear rate.. Equivalently, the particle Weissenberg number $Wi = \tau_{relax}\dot{\gamma}$ also captures particle deformation and Wi is used in this study. For $Wi > 1$, the shear force overcomes particle elastic contraction and strongly deforms the particle. The flow field around a stretched, elastically contracting soft particle near the wall results in a net migration force that pushes it away from the wall. [20–23]

In addition, particle inertia in flow also leads to migration for finite particle Reynolds number $Re = \rho\dot{\gamma}R^2/\eta \geq 1$, where ρ is the fluid density.[24–27] Re is characterized by the fluid

[a] *Institute of Physics, Academia Sinica, Taipei, 11529 Taiwan. E-mail: yenglong@phys.sinica.edu.tw*
[b] *Department of Chemical Engineering, National Tsing-Hua University, Hsinchu, Taiwan.*
[c] *Department of Physics, National Taiwan University, Taipei, Taiwan.*

velocity difference across the particle $\delta U = \dot{\gamma} R$. It has been shown that the difference between fluid velocity at the particle surface and the particle velocity results in a particle surface stress leading to cross-stream lateral migration.[28] In simple shear flow, the migration force pushes the particle towards the steady state position at the channel center. In Poiseuille flow the steady state position is off-center due to the curvature of the flow velocity profile.

To understand the role of deformation- and inertia-driven migration of soft particle suspensions, one needs to account for not only how particle motion perturbs the fluid, but also particle deformation due to fluid shear and hydrodynamic perturbations. Boundary integral formulation have extensively studied droplet dynamics in Stokes flow[29–35]. However, accurately modeling the interplay between particle deformation and the fluid field can require a very fine surface mesh and is very computationally expensive. Particle deformation and dynamics are coupled with the hydrodynamic field need to be resolved simultaneously. Recent advances in multi-scale approaches such as the immersed boundary method (IB) [36–38], multi-particle collision method (MPC)[39–41], dissipative particle dynamics (DPD)[42,43] and lattice Boltzmann (LB)[44–48] have significantly improved the efficiency of complex fluid flow modeling based on individual particles. In this study, we employ a combination of LB and IB to study the lateral migration of a particle in simple shear and Poiseuille flow.

2 Method

We developed a coarse-grained model combining Lagrangian particle dynamics[49] and Eulerian LB fluid through immersed boundary method (IB).[36,46,47,50,51] The method has been shown to capture the physical characteristics of particle deformation in shear flow, inter-particle hydrodynamic forces, and the near-wall hydrodynamic field around a shear-deformed particle. [20] In order to understand the effects of shear-induced near-wall deformation- and inertia-driven particle migration, we examine particle migration in the simple scenario of a single particle in shear flow and Poiseuille flow between two parallel plates with height $H = 16R$. An ensemble of one hundred particle trajectories is performed until the particle distance from the wall reaches steady state, from small to moderate Wi and Re. Particle and fluid fluctuations are not included in order to directly determine the particle migration velocities.

LB is carried out on a three-dimensional cubic lattice with 19 discrete velocities (the D3Q19 model). The lattice spacing is Δx, the kinematic viscosity is $\nu = \eta/\rho = 1/6[\Delta x^2/\Delta\tau]$, and $\Delta\tau$ is the LB time step. Details of the LB method can be found in recent reviews [45,52]. LB models a compressible fluid, where the fluid density could vary significantly at high velocities if the Mach number $Ma = v_{fluid}/v_{sound} \to 1$. The error due to fluid compressibility is of order (Ma^2). In this study, the fastest fluid velocities are kept to $Ma < 0.4$. The systemic errors are considered by comparison to theoretical predictions.

The coarse-grained soft particle is constructed by accounting for the membrane elasticity with a two-dimensional closed network of beads and springs. The beads interact with each other via purely repulsive Weeks-Chandler-Andersen (WCA) potential, given by

$$U_{\mathrm{WCA}}(r) = \begin{cases} 4\varepsilon\left[\left(\frac{\sigma}{r}\right)^{12} - \left(\frac{\sigma}{r}\right)^{6} + \frac{1}{4}\right] & r < 2^{1/6}\sigma, \\ 0 & r > 2^{1/6}\sigma. \end{cases} \quad (1)$$

Neighboring beads are connected with finitely extensible nonlinear elastic (FENE) spring, given by

$$U_{\mathrm{FENE}}(r) = -\frac{kl_0^2}{2}\ln\left[1 - \left(\frac{r}{l_0}\right)^2\right], \qquad r < l_0. \quad (2)$$

which is harmonic at small separation but restricts the separation to within l_0. The parameters of the potentials are chosen to be $\sigma = \Delta x$, $l_0 = 3\Delta x$, $\varepsilon = k_{\mathrm{B}}T$. The spring constant $k\sigma^2 = 0.017, 0.17$, and $2.83\Delta\varepsilon$ are chosen for particles with different stiffness. $\Delta\varepsilon$ is the simulation energy unit.

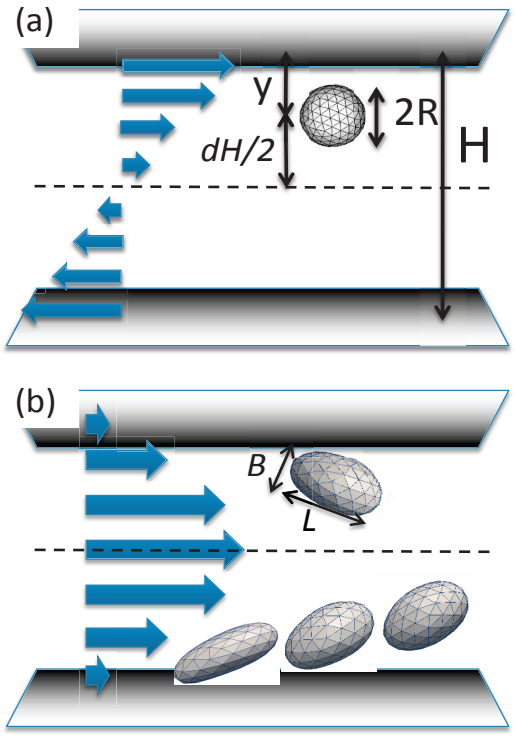

Fig. 1 Illustration of (a) a hard sphere in simple shear flow at a position y from the wall, and its relative distance from the center is $d = (1 - 2y/H)$. (b) A deformed particle with long axis L and short axis B in Poiseuille flow between 2 parallel plates.

Bead positions on the spherical shell are acquired by triangle tessellation, as shown in Fig. 1. The radius of the sphere is $R = 3.2\Delta x$. A bending potential is imposed between all neighboring triangular faces

$$U_{\text{bend}} = k_{\text{bend}}\,(1-\cos\theta)\,, \tag{3}$$

where θ is the angle between the surface normals of two neighboring faces. $k_{\text{bend}} = 0.056, 0.56, 2.83\Delta\varepsilon$ are used for $k\sigma^2 = 0.017, 0.17, 2.83$, respectively. These parameters are chosen such that the ratio between the bending and the elastic moduli, characterized by the Föppl-von Kármán number $Fv = GR^2/k_{\text{bend}}$, is less than 100 to ensure the buckling modes of the coarse-grained particle are dampened.[53,54]

The triangular bending force is exerted on the four beads with positions $\mathbf{r}_1, \mathbf{r}_2, \mathbf{r}_3, \mathbf{r}_4$ that constitute two adjacent triangles $\mathbf{r}_1 - \mathbf{r}_2 - \mathbf{r}_3$ and $\mathbf{r}_2 - \mathbf{r}_1 - \mathbf{r}_4$. The bending forces on each bead are given by

$$\mathbf{F}_1 = \frac{k_{\text{bend}}}{\sigma}\frac{(\mathbf{r}_4-\mathbf{r}_3)\cdot\mathbf{a}}{n_1}\hat{\mathbf{n}}_1 \tag{4a}$$

$$\mathbf{F}_2 = \frac{k_{\text{bend}}}{\sigma}\frac{(\mathbf{r}_4-\mathbf{r}_3)\cdot\mathbf{a}}{n_2}\hat{\mathbf{n}}_2 \tag{4b}$$

$$\mathbf{F}_3 = \frac{k_{\text{bend}}}{\sigma}\left[\frac{(\mathbf{r}_1-\mathbf{r}_4)\cdot\mathbf{a}}{n_1}\hat{\mathbf{n}}_1 + \frac{(\mathbf{r}_2-\mathbf{r}_4)\cdot\mathbf{a}}{n_2}\hat{\mathbf{n}}_2\right] \tag{4c}$$

$$\mathbf{F}_4 = \frac{k_{\text{bend}}}{\sigma}\left[\frac{(\mathbf{r}_3-\mathbf{r}_1)\cdot\mathbf{a}}{n_1}\hat{\mathbf{n}}_1 + \frac{(\mathbf{r}_3-\mathbf{r}_2)\cdot\mathbf{a}}{n_2}\hat{\mathbf{n}}_2\right], \tag{4d}$$

where $\mathbf{n}_1 = (\mathbf{r}_3-\mathbf{r}_1)\times(\mathbf{r}_4-\mathbf{r}_1)$, $\mathbf{n}_2 = (\mathbf{r}_4-\mathbf{r}_2)\times(\mathbf{r}_3-\mathbf{r}_2)$, and $\mathbf{a} = \hat{\mathbf{n}}_2\times\hat{\mathbf{n}}_1$. The sign of θ is given by $\sin\theta = (\hat{\mathbf{n}}_2\times\hat{\mathbf{n}}_1)\cdot\hat{\mathbf{e}}$, where $\mathbf{e} = \mathbf{r}_4-\mathbf{r}_3$, then $\mathbf{a} = \sin\theta\hat{\mathbf{e}}$. Eq. (4) has the expected directionality for a force that only affects the angle but does not affect the translation, rotation, and shape of the two triangles.

The particle volume and total surface area are conserved by applying an isotropic pressure $P_V(t)$ and a surface dilatation tension k_A on the particle, given by

$$P = F_V(t)/A = [k_V(V(t)-V_0)/V_0]/A \tag{5a}$$

$$F_A(t) = k_A(A(t)-A_0)/A_0 \tag{5b}$$

where $V(t)$ and V_0 are the instantaneous and the rest particle volume, and $A(t)$ and A_0 are the instantaneous and rest surface area. The constraint forces F_V and F_A are distributed equally on all the beads that constitute the particle surface. For the softest particle examined here, it was found that with $k_V = 0.56\Delta\varepsilon/\Delta x$ and $k_A = 0.56\Delta\varepsilon/\Delta x$, the particle volume and area can vary up to 10% at the highest shear rate examined. The total conservative forces acting on each bead is given by $\mathbf{F}^{\mathbf{C}} = -\nabla U = F_{\text{WCA}} + F_{\text{FENE}} + F_{\text{bend}} + F_V + F_A$. All beads have mass $m_{\text{b}} = 36m_0$, where m_0 is the simulation unit mass. The velocity Verlet method is employed to project the bead trajectories with the time step $\delta t = 0.1\Delta\tau$.

The shape of the particle is characterized by the Taylor deformation parameter $D = (L-B)/(L+B)$, where L and B are the longest and shortest particle axes during deformation, as shown in Fig. 1b. The particle elasticity is characterized by the surface elastic modulus G=stress/strain=$\delta f_x/\delta R_x$, in unit of $\Delta\varepsilon/\Delta x^2$. f_x is an external stretching force in the x-direction and δR_x is the particle deformation along the direction of the applied force. The orthogonal elastic modulus $\delta f_x/\delta R_z$ is also measured. The particle elasticity is also characterized by its deformation relaxation time τ_{relax}, measured from the relaxation of the particle stretch after shear deformation by fitting $[L(t)-L_{eq}]^2$ to $\exp(-2t/\tau_{\text{relax}})$. Fig. 2a shows that $G \sim k^{0.7\pm0.05}$. The inset shows that $Fv < 100$ for the regime investigated in this study and particle buckling is not significant. G is also found to very weakly depend on k_{bend}, k_V and k_A. The elastic relaxation time $\tau_{relax} \sim G^{-1.1\pm0.1}$ is also observed, which give an approximate relation between Ca and Wi, with $Wi \approx 15Ca$.

The particle deformation D is known to be linearly dependent on Ca under small shear for droplets and elastic capsules.[22,29] For the elastic particles considered in this study, D is observed to be linearly proportional to Wi only for $Wi < 1$, and D reaches a plateau under strong shear as the particle stretches in the non-linear elasticity regime, as shown in Fig. 2b. The inset shows that $D \approx (25/4)Ca$, which agrees with theoretical prediction. [29] Under simple shear flow, the particle deformation is constant throughout the channel except near the wall.

Hydrodynamic interactions is captured with the exchange and propagation of frictional momentum between the fluid and the DP[45,55]. Each bead on the DP experiences a friction force

$$\mathbf{F}_f = -\zeta[\mathbf{u}_b(\mathbf{r}_b) - \mathbf{u}_f(\mathbf{r}_b)] \tag{6}$$

where $\mathbf{u}_b(\mathbf{r}_b)$ and $\mathbf{u}_f(\mathbf{r}_b)$ are the bead and fluid velocity at the bead position $\mathbf{r}_b$, respectively, and $\zeta = 3\pi\eta\sigma = 56.4m_0/\Delta\tau$ is the bead friction coefficient. The fluid velocity at position $\mathbf{r}_b$ is determined by a trilinear interpolation of the fluid velocity on the neighboring lattice points nn that enclose $\mathbf{r}_b$, $\mathbf{u}_f(\mathbf{r}_b) = \sum_{\mathbf{r}\in nn} w_{\mathbf{r}}\mathbf{u}(\mathbf{r})$, where the weights $w_{\mathbf{r}}$ are the coefficients of the normalized linear Lagrange interpolation polynomial. The frictional momentum density $\Delta\mathbf{j} = -\mathbf{F}_f\delta t/\Delta x^3$ is transferred to the fluid.

The beads are repelled from the walls with a repulsive potential when the beads are within $1\Delta x$ of the walls. The particle elasticity and fluid velocity are independently varied in order to investigate the contributions of particle inertia and particle deformation to particle migration. Three types of soft particles, with the two-dimensional elasticity $G = 0.4$, 4.4, and 44.0 $\Delta\varepsilon/\Delta x^2$ are chosen to identify the hydrodynamically-induced migration fluxes due to particle inertia and deformation. With the simulation energy ($\Delta\varepsilon$) matched to the thermal energy at room temperature and $\Delta x = 1\mu m$, the elasticities cor-

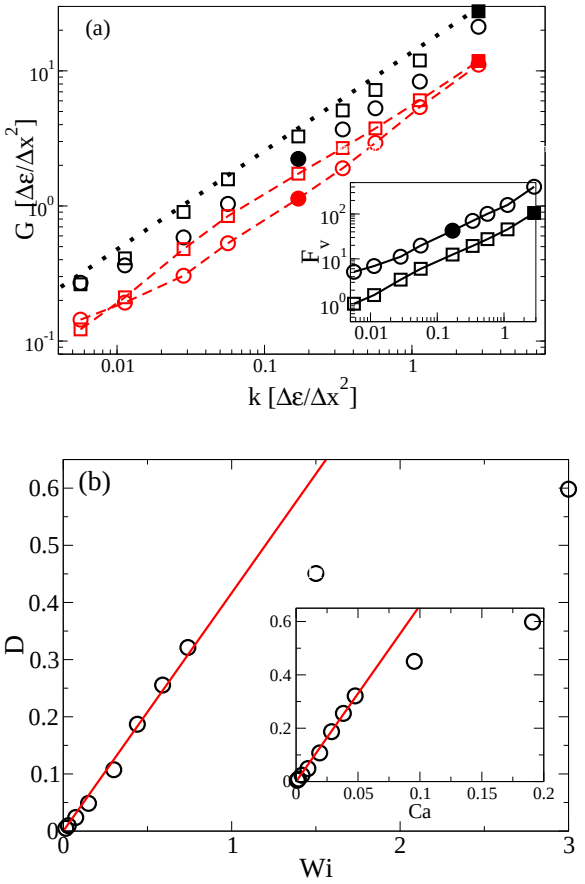

Fig. 2 (a) Particle long (symbols) and short (symbols with dashed line)axis stretch elasticity as function of the spring constant for $k_{bend} = 0.56$ (circles) and $k_{bend} = 2.83$ (squares). The solid symbols indicate the chosen parameters for the hard and soft spheres examined here. The dotted line shows the power law fit with $G \sim k^{0.7}$. The inset shows Fv as a function of k. (b) Particle deformation as a function of Wi and Ca (inset).

respond to 0.29, 2.9, and $29\mu N/m$. For $\Delta x = 100\mu m$, the elasticities correspond to 2.9, 29, and $290mN/m$. For comparison, the elasticity of a red blood cell (diameter $\approx 6-8\mu m$) is $\approx 6\mu N/m$ and the surface tension of water in air is $\approx 72mN/m$. The elastic properties of soft particles with size range between μm and mm can be captured with the coarse-grained particle model.

With the assumptions involved in LB and IB, systemic errors can arise due to fluid compressibility and the momentum transfer between the particle and the fluid. With the immersed boundary method, the no-slip boundary condition is imposed on the particle surface, and the friction momentum is calculated based on first-order Lagrange interpolation of the fluid velocity at the bead position from the lattice fluid velocity. Thus, the accuracy of momentum coupling is of $O(\Delta x^2)$. Furthermore, the fluid velocity from LB is of $O(\Delta x^2)$ accuracy. The systemic error may be estimated by examining the velocity field generated by a moving particle with velocity U_p in a quiescent fluid inside a periodic domain. Comparison of the LB-IB solution is made with the results using the lattice Boltzmann method with the fluid bounce-back condition (LB-BB) at the fluid-particle interface. The accuracy of LB-BB has been well characterized for colloidal hydrodynamics, and it was found to accurately capture the drag force acting on a colloid in flow up to particle Reynolds number $Re_p = \rho U_p R/\eta \approx 100$.[56,57] The fluid velocity field along the direction orthogonal to the particle velocity is calculated using LB-IB and LB-BB. Fig. 3 shows that the results quantitatively agree for the range of particle velocities relevant to this study. This shows that the immersed boundary method captures the fluid velocity field with the same order of accuracy as the bounce-back condition. Furthermore, Fig. 3 shows that the fluid field agree quantitatively with the prediction by Hasimoto [58] for a point particle in Stokes flow in a periodic domain for $Re_p = 0.29$. At higher Re_p, the reduced fluid velocity correspond to a increase in the fluid boundary layer around the spherical particle. Fluid density variation inside and outside the particles at the highest flow rates studied were found to be less than 0.1 percent.

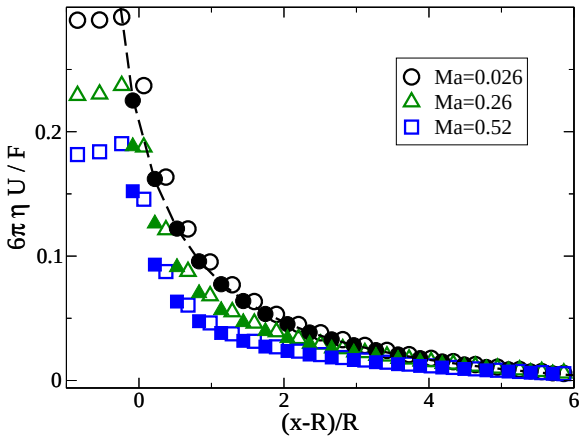

Fig. 3 Fluid velocity field along the velocity-normal at distance $(x-R)/R$ from a moving particle with velocity $\mathbf{U}_p = U_p\hat{\mathbf{y}}$. U_p is chosen with Mach number $Ma = 0.026$ (circles), 0.26(triangles), 0.52 (squares), corresponding to $Re_p = 0.29, 2.9, 5.8$. Results from LB-IB are shown in empty symbols, and the results from LB-BB are shown in filled symbols. Prediction for a periodic point force is shown as the dashed line.

3 Migration of hard and soft particles

We first examine the lateral migration of hard spheres. Shear-induced inertial migration of hard spheres has been well-studied experimentally and theoretically. [22,25,28,59] For small but finite Re, the unbalanced surface stress due to particle inertia leads to particle migration away from a wall boundary. In contrast, a hard sphere in Stokes flow ($Re = 0$) does not migrate. The inertia-driven migration effect has been exploited to separate particles of different sizes and shapes. [22,24,25,59,60] First order theoretical analysis of the Navier-Stokes equation in the limit of $Re < (R/H)^2$ shows that the migration velocity v_{lift} is proportional to Re [28], given by

$$\frac{v_{lift}}{v_m} = \frac{1}{6\pi}\frac{R}{H}Re[G_1(d) + \alpha G_2(d)] \quad (7)$$

where $v_m = v_{wall}, \alpha = 0$ for simple shear flow and $v_m = v_{max}, \alpha = -4$ for Poiseuille flow. $G_1(d)$ and $G_2(d)$ are numerically integrated functions from the particle surface stress. [28] In simple shear flow, the lift velocity is expected to be linearly dependent on the the particle distance from the channel center ($d = 1 - 2y/H$) as the particle approaches center, with steady state position at the center where $v_{lift} = 0$. In Poiseuille flow, the lift velocity is expected to quadratically vary with d, with zero crossings and steady state positions at $d = 0.6$ and -0.6.

LB-IB is employed to examine particle migration under simple shear flow and Poiseuille flow. First, the predictions for hard spheres are tested with a very stiff particle with $G = 44\Delta\varepsilon/\Delta x^2$ with moderate Re and negligible Wi. Under simple shear flow, Fig. 4a shows the migration velocity is linearly dependent on d for $d < 0.6$ at lower Re, and the particle steady state position is at the center. For $Re < 0.1$, the observed v_{lift} from LB-IB are in quantitative agreement with eq. 7. Quantitative agreement is also found with the results of LB-BB up to $Re = 0.32$. As Re increases, it is observed that the relative migration velocity does not increase linearly with Re. Furthermore, v_{lift} is found to become quadratically dependent on d with the steady state position at the center, which is captured by both LB-IB and LB-BB. These differences with eq. 7 may be due to higher order inertial effects since the first order analysis is strictly valid for $Re < (R/H)^2$. For comparison to experiments with 10 and 100μm particles, the shear rates for $Re = 1$ are 10^4 and $100s^{-1}$, respectively.

Under pressure-driven flow, v_{lift} is found to have quadratic dependence on d for $d < 0.6$ for the entire range of Re examined. LB-IB results agree quantitatively with $O(Re)$ analysis for $Re = 0.032$ and 0.16. It is observed that particles near the central region will migrate towards the walls due to the negative v_{lift}, and the steady state position at $d = 0.6$ does not vary with Re even for Re much larger than $(R/H)^2$ as predicted. For the results of LB-BB, more velocity oscillations are found due to errors caused by the first order bounce back condition.

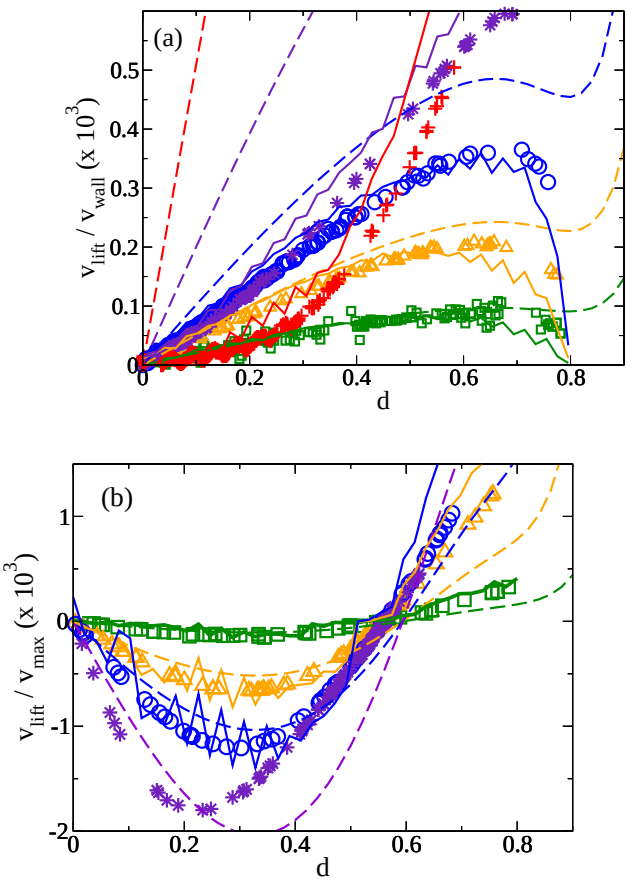

Fig. 4 Lift velocity of a hard sphere with $G = 44\Delta\varepsilon/\Delta x^2$ in (a) simple shear for $Re = 0.028$ (squares), 0.07 (triangles), 0.14 (circles), 0.28 (*), 0.7 (+) and (b) pressure-driven flow for $Re = 0.032$ (squares), 0.16 (triangles), 0.32 (circles), 0.65 (*) from the composition of 100 initially randomly placed spheres. Corresponding solid lines are the results of LB-BB. Dashed lines show the predicted v_{lift} from eq. 7 ordered from bottom to top for low Re to higher Re.

In the other limiting regime where particle inertia is small and particle deformation is large, particle migration is driven by deformation-induced hydrodynamic forces near a wall. Under pressure-driven flow, DP deformation depends on the local shear force and varies linearly as the particle migrates towards the center at small shear rates, as shown in Fig. 5. At higher Wi, particle deformation D plateaus near the wall, where the shear rate is the highest, due to the non-linear elastic spring. For $Wi = 6.9$, the highest shear rate examined, the particle stretches nearly 100%. Under simple shear flow, the local shear rate is constant throughout the channel and the steady state particle shape does not change except near the wall. Prior studies have measured the migration velocity [22,23,38,61]. Under simple shear flow, the migration velocity for droplets with

equal inner and outer viscosity is found to be

$$\frac{v_{lift}}{v_{wall}} = 1.1D\left(\frac{R}{H}\right)^3 d[1+\frac{8}{(1-d^2)^2}] \quad (8)$$

The prefactor depends on the ratio between the inner and outer fluid viscosity of the particle. To examine particle migration in the deformation-dominated regime, the migration trajectories of a softer particle with $G = 0.4$ are examined. v_{lift} exhibits quadratic dependence on d as shown in Fig. 6a, as expected from eq. 8. The lift velocity for $Wi = 0.15$ and 0.3 agree quantitatively with eq. 8, but v_{lift}/v_{wall} does not increase proportionally with Wi as the shear rate further increases. This may be due to the non-linear dependence of particle deformation on shear force for large particle deformations, higher order Wi contributions, and the increased effect of inertia driven migration.

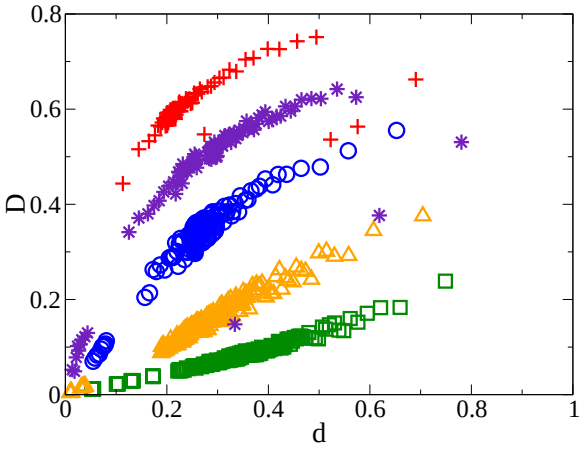

Fig. 5 Deformation of soft particles with $G = 0.4\Delta\varepsilon/\Delta x^2$ under pressure-driven flow for $Re = 0.033$ (squares), 0.065 (triangles), 0.165 (circles), 0.33 (*), 0.65 (+) and $Wi = 0.35$, 0.7, 1.7, 3.5, 6.9 ordered from bottom to top. The data set is from the composition of 50 initially randomly placed spheres. Data point spread is due to initial particle shape change from sphere to ellipsoid under shear.

Under Poiseuille flow, Fig. 6b shows that the particle migration velocity have non-linear dependence on d for $Wi < 1.0$, and v_{lift} decays to 0 as d approaches 0 as shown in . First order analysis has found the lateral migration velocity to be [23]

$$\frac{v_{lift}}{v_{max}} = 1.3D\left(\frac{R}{H}\right)^2 d \quad (9)$$

From Fig. 5, it is observed that D decays linearly as d approaches 0. This dependence combined with eq. 9 shows that v_{lift} should decay quadratically near the channel center.[22,23,38,61] However, Fig. 6b shows that the observed migration velocity increases faster than the quadratic dependence on d for $d > 0.4$. This cannot be simply explained by the non-linear elastic particle deformation near the wall. Indeed, the non-linear elastic deformation near the wall should lead to a weaker dependence on d instead of higher order dependence. The stronger measured migration velocity may be due to additional contributions to particle migration due to the particle inertia. However, simply adding the inertial migration contribution from eq. 7b does not lead to better agreement with the measured migration velocity. Further analysis starting from the migration velocity of a droplet near a wall [22,61] and extending to a particle in Poiseuille flow between two parallel plates results in

$$\frac{v_{lift}}{v_{max}} = 9D\left(\frac{R}{H}\right)^3 \frac{d(1+d^2)}{(1-d^2)^2} \quad (10)$$

As shown in Fig. 6b, the additional dependence on $(1+d^2)/(1-d^2)^2$ appears to account for the stronger dependence for a particle closer to the wall. The observed v_{lift} qualitatively agrees with eq. 10 for $Wi < 1$, with the observed v_{lift} larger than eq. 10 by a factor of 2.

At high Wi where the particle is strongly deformed near the wall, it is found that closer to the wall, the dependence of v_{lift} on d decreases. This is consistent with the smaller changes in the particle deformation at higher shear rates near the wall, and leading to weaker dependence of v_{lift} on d. In addition, v_{lift} becomes negative as the particle approaches the channel center, showing a migration flux away from the center for particles near the center. This may be attributed to inertia-driven particle migration away from the center at the higher shear rates, where negative v_{lift} is found near the channel center as shown for hard spheres. Furthermore, as the particle moves cross-stream towards the center, the projected cross-stream surface area ($A_{xz} = \sum \mathbf{n}_i \cdot (\hat{x}+\hat{z})$) decreases as the particle shape becomes less deformed. This leads to a gradient in the migration friction and a migration flux away from the center. The position at which $v_{lift} = 0$ also shifts towards the channel center as the shear rate increases, which is due to the change in the particle deformation for different Wi. This is in contrast to hard sphere migration for which the steady state position is independent of Re in Poiseuille flow.

We further examine particle migration under simple shear and Poiseuille flow chosen such that $Re \sim Wi < 1$ for soft particles with $G = 4.4\Delta\varepsilon/\Delta x^2$. In simple shear flow, the linear combination of eqs. 7 and 8 is in quantitative agreement with the observed v_{lift} at low shear rates as shown in Fig. 7a. Quadratic dependence of v_{lift} on d is found for $Wi > 0.3$, where the particle is stretched by $\approx 10\%$. For $Re = 0.7$ and $Wi = 0.74$, v_{lift} is found to quadratically decrease to zero at $y/H \approx 0.3$ and $v_{lift} = 0$ in the central region for $d < 0.35$. In this region, there is no observed net lift force about the particle and the particle migrates neither towards nor away from the center. Indeed, for $Wi > 0.3$, the migration-free region is

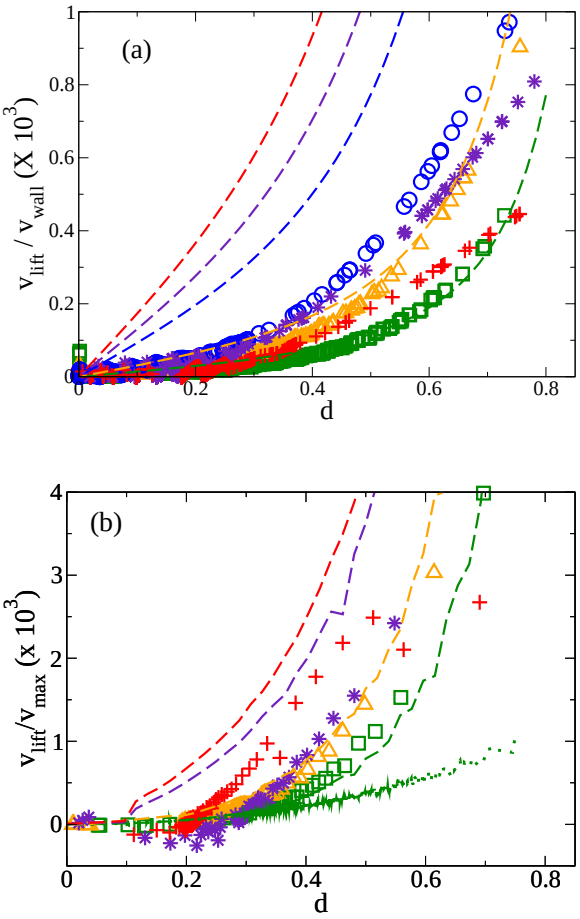

Fig. 6 Lift velocity of a deformable particle with $G = 0.4\Delta\varepsilon/\Delta x^2$ in (a) simple shear $Re = 0.014$ (squares), 0.028 (triangles), 0.07 (circles), 0.14 (*), 0.28 (+) and $Wi = 0.15$, 0.3, 0.74, 1.5, and 3.0. Dashed lines are the predictions of eq. 8 ordered from bottom to top for low Re to higher Re. (b) In pressure-driven flow for $Re = 0.033$ (squares), 0.065 (triangles), 0.33 (*), 0.65 (+) and $Wi = 0.35$, 0.7, 1.7, 3.5, 6.9, from the composition of 50 initially randomly placed spheres. The dashed lines show eq. 10 multiplied by a factor of 2 for the same Wi, ordered from bottom to top. The dotted line shows eq. 9 for $Wi = 0.35$.

found to expand from the channel center as the shear rate increases, as shown in Fig. 8. This is in stark contrast to the inertia-dominated or deformation-dominated lateral migration in simple shear flow, where the particle migrate to the channel center. It also differs from purely inertia or deformation-driven migration results found in Poiseuille flow, where the particles migrate to a specific position in the channel. One possible explanation for the "migration-free" zone may be the rotating motion of the particle surface. At all Wi examined here, the soft particle appears to undergo tank-treading motion in simple shear flow. It has been previously suggested that tank treading motion of an ellipsoidal particle also induces a migration flux. [62,63] For the higher Wi where the particle does not migrate, they appear to simply tank-tread at an inclined angle, without lateral migration. The tank-treading frequency is proportional to the shear rate, reaching as high as $10^{-2}[1/\Delta\tau]$. The fluid perturbations due to tank treading motion at high frequency may overcome the inertia- and deformation-driven fluid stress gradient.

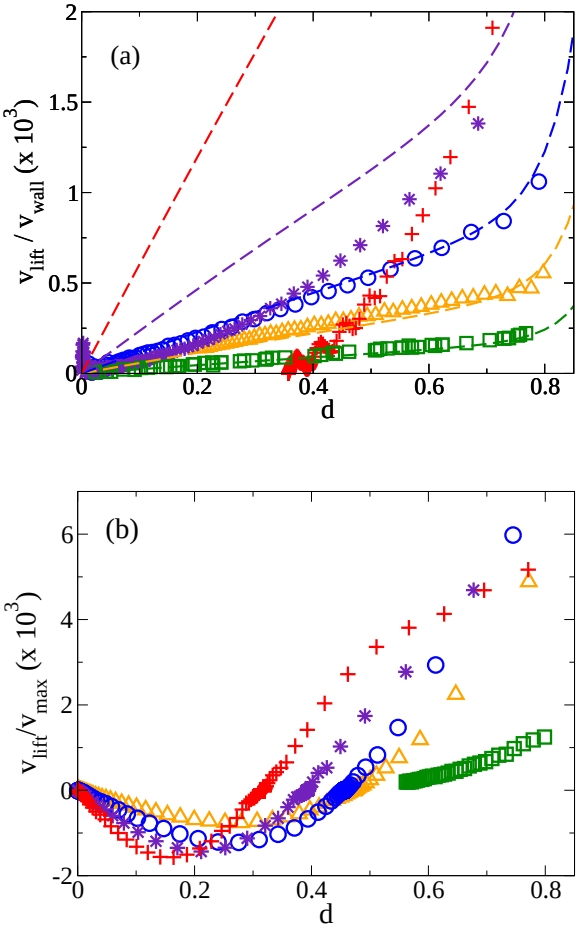

Fig. 7 Lift velocity of a deformable particle with $G = 4.4\Delta\varepsilon/\Delta x^2$ in (a) simple shear for $Re = 0.028$ (squares), 0.07(triangles), 0.14 (circles), 0.28 (*), 0.7 (+) and $Wi = 0.03$, 0.074, 0.15, 0.3, and 0.74. Dashed lines show the linear combinations of eqs. 7 and 8, ordered from bottom to top. (b) pressure-driven flow for $Re = 0.033$ (squares), 0.065 (triangles), 0.33 (circles), 0.65 (*), 0.98 (+) and $Wi = 0.035$, 0.17, 0.35, 0.70, 1.05. The figures are overlaid composition of 100 trajectories of initially randomly placed spheres.

Under Poiseuille flow, soft sphere migration velocity is quadratically dependent on d, similar to hard sphere migration at small Wi and Re. The position at which v_{lift} crosses zero shifts towards the center as the shear rate increases in contrast

to inertia-driven migration of hard spheres. For $Wi = 1.05$, v_{lift} appears to decrease linearly near the wall for $d > 0.5$, and quadratically as the particle migrates closer to the channel center. These differences may be attributed to particle deformation due to the shear force, and also the change of the particle shape as the local fluid shear force decreases as the particle moves from the wall towards the center. Near the wall, the shear force is the strongest and the particle is deformed to an ellipsoid. As the particle approaches the center, it becomes more spherical. The change of particle shape introduces a deformation-dependent particle drift away from the channel center, which is more pronounced for softer particles.

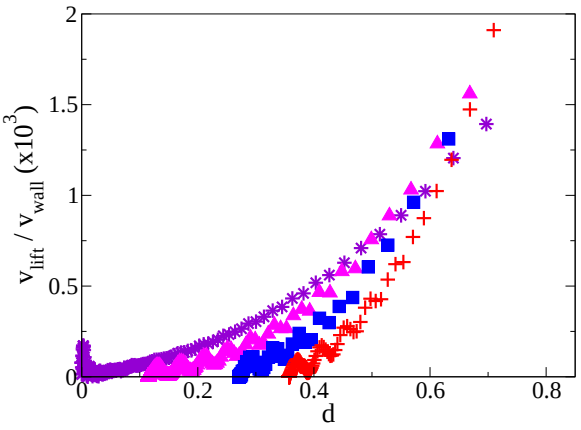

Fig. 8 Lift velocity of a deformable particle with $G = 4.4\Delta\varepsilon/\Delta x^2$ in simple shear for $Re = 0.28$ (*), 0.42 (solid triangles), 0.56 (solid squares), and 0.74 (+) and $Wi = 0.3$, 0.44, 0.59, 0.74.

4 Conclusion

For droplets, vesicles, and capsules, inertial and deformation-driven migration away from the channel walls in microfluidic flow may be utilized to separate particles based on size and deformability. It is interesting to observe that particle migration velocity in Poiseuille flow is 3 to 4 times faster than in simple shear flow for hard and soft particles, which is due to the larger fluid velocity change across the particle. This study also found that for small Reynolds and Weissenberg number flow, the particle migration velocities are quantitatively captured by first-order analysis of the Navier-Stokes equation in shear flow. For hard spheres, theoretical analysis also captures the migration velocity in Poiseuille flow. For very soft particles, the predictions of the deformation-driven particle migration velocity in pressure-driven flow show a weaker dependence on d than observed, but analysis based on the migration velocity near a surface appears to be qualitatively consistent with the observed migration velocity. For soft particles in shear flow, the linear combination of the $O(Re)$ and $O(Wi)$ predictions captures the particle migration velocities under conditions where particle inertia and deformation are small but not negligible.

At moderate Re and Wi, it is found that the particle migration velocities for hard and soft particles are smaller than expected and do not increase linearly with Re and Wi. The qualitative dependence of the migration velocity on the particle distance from the channel center also changes as Re approaches 1 and as Wi approaches 1. Under simple shear flow, the migration velocity of a hard sphere has non-linear dependence on d. For soft particles, the migration velocity becomes zero in a central migration-free region. The steady state position of the particles remain at the channel center or in the central region. It is suspected that this may be due to a combination of (1) contributions from higher order inertia- and deformation-driven flux, (2) fluid boundary layer around the particle increaseat higher Re, (3) fluid field perturbation due to particle tank-treading motion and (4) systemic errors due to high fluid velocity. The cause will be investigated in future studies.

Under pressure-driven flow, the steady state position of a hard sphere is found to be weakly dependent or independent on Re. For soft particle, the steady state position moves towards the center as the shear rate and particle deformation increases. This indicates that particles with different elasticities can be separated by their distance from the center-line. For hard spheres, different species with the same size will not be separated in the stream, but particles of different sizes and shapes may be separated. For soft spheres of the same size but different elasticities, increased particle deformation results in a steady state position closer to the center. With the parabolic flow profile, this means that the soft particles would travel at different velocities, which is being exploited for cell and particle flow-based fractionation in microfluidic devices.

5 Acknowledgments

Funding for this study comes from the Academia Sinica Career Development Award 100-CDA-M01 and the Republic of China National Science Council project 101-2112-M01-03-MY3. Support also came from NCTS Taiwan. I would also like to thank Dr. D. Leighton, Dr. H.C. Chang, Dr. C.S. Hur, Dr. M. Dao, and Dr. Z. Peng for their help and support through many discussions.

References

1 R. Fåhraeus and T. Lindqvist, *Amer. J. Physiol.*, 1931, **96**, 562.
2 J. Vermant and M. Solomon, *J. Phys.: Condens. Matter*, 2005, **17**, R187.
3 E. Nazockdast and J. F. Morris, *Soft Matter*, 2012, **8**, 4223.
4 S. Chien, S. Usami and R. Skalak, *Handbook of Physiology - The Cardiovascular System*, American Physiological Society, 1984, vol. IV, p. 217.
5 A. S. Popel and P. C. Johnson, *Annu. Rev. Fluid Mech.*, 2005, **37**, 43–69.
6 H. H. Lipowsky, *Microcirculation*, 2005, **12**, 5.

7 C. Pozrikidis, *Modeling and Simulation of Capsules and Biological Cells*, Chapman & Hall/CRC, London, 1st edn, 2003, vol. 2.
8 A. Kumar and M. D. Graham, *Phys. Rev. E*, 2011, **84**, 066316.
9 A. Kumar and M. D. Graham, *Phys. Rev. Lett.*, 2012, **109**, 108102.
10 H. Zhao, A. P. Spann and E. S. G. Shaqfeh, *Phys. Fluids*, 2011, **23**, 121901.
11 H. Zhao, E. S. G. Shaqfeh and V. Narsimhan, *Phys. Fluids*, 2012, **24**, 011902.
12 P. Garstecki, I. Gitlin, W. DiLuzio, G. M. Whitesides, E. Kumacheva and H. A. Stone, *Appl. Phys. Lett.*, 2004, **85**, 2649–2651.
13 H. L. Goldsmith, G. R. Cokelet and P. Gaehtgens, *Amer. J. Physiol.*, 1989, **257**, H1005–H1015.
14 H. Goldsmith and R. Skalak, *Annu. Rev. Fluid Mech.*, 1975, **7**, 213.
15 J. J. Bishop, P. R. Nance, A. S. Popel, M. Intaglietta and P. C. Johnson, *Amer. J. Physiol.*, 2001, **280**, H222–H236.
16 B. P. Helmke, M. Sugihara-Seki, R. Skalak and G. W. Schmid-Schoenbein, *Biorheology*, 1998, **35**, 437.
17 L. L. Munn, R. J. Melder and R. K. Jain, *Biophys. J.*, 1996, **71**, 466.
18 A. Kumar and M. D. Graham, *Soft Matter*, 2012, **8**, 10536.
19 J. B. Freund and M. Orescanin, *J. Fluid. Mech.*, 2011, **671**, 466–490.
20 C. Hsu and Y.-L. Chen, *J. Chem. Phys.*, 2010, **133**, 034906.
21 J. R. Smart and D. T. Leighton, *Phys. Fluids*, 1991, **3**, 21.
22 A. Karnis and S. G. Mason, *J. Colloid Interf. Sci.*, 1967, **24**, 164.
23 P. C. H. Chan and L. G. Leal, *J. Fluid Mech.*, 1979, **92**, 131–170.
24 S. C. Hur, H. T. Tse and D. Di Carlo, *Lab Chip*, 2010, **10**, 274.
25 G. Segre and A. Silberberg, *Nature*, 1961, **189**, 209.
26 A. Karnis, S. G. Mason and H. L. Goldsmith, *Nature*, 1963, **200**, 159.
27 E. J. Lim, T. J. Ober, J. F. Edd, G. H. McKinley and M. Toner, *Lab Chip*, 2012, **12**, 2199.
28 B. P. Ho and L. G. Leal, *J. Fluid Mech.*, 1974, **65**, 365.
29 D. Barthès-Biesel and J. M. Rallison, *J. Fluid Mech. Digital Archive*, 1981, **113**, 251.
30 E. Lac, A. Morel and D. Barthès-Biesel, *J. Fluid Mech.*, 2007, **573**, 149.
31 C. Pozrikidis, *Ann. Biomed. Eng.*, 2003, **31**, 1194.
32 C. Pozrikidis, *Phys. Fluids*, 2005, **17**, 031503.
33 C. Pozrikidis, *Ann. Biomed. Eng.*, 2005, **33**, 165–178.
34 A. Kumar and M. D. Graham, *J. Comp. Phys.*, 2012, **231**, 6682.
35 C. Pozrikidis, *Computational Hydrodynamics of Capsules and Biological Cells*, Chapman & Hall/CRC, London, 1st edn, 2010.
36 C. Peskin, *Acta Numerica*, 2002, 1.
37 S. K. Doddi and P. Bagchi, *Phys. Rev. E*, 2009, **79**, 046318.
38 S. K. Doddi and P. Bagchi, *Int. J. Multiphase Flow*, 2008, **34**, 966–986.
39 G. Gompper, T. Ihle, D. Kroll and R. Wrinkler, *Adv. Polym. Sci.*, 2009, **221**, 1.
40 H. Noguchi and G. Gompper, *Phys. Rev. Lett.*, 2007, **98**, 128103.
41 H. Noguchi and G. Gompper, *Proc. Natl. Acad. Sci. U.S.A.*, 2005, **102**, 14159–14164.
42 I. V. Pivkin and G. E. Karniadakis, *Phys Rev Lett*, 2008, **101**, 118105.
43 D. A. Fedosov, W. Pan, B. Caswell, G. Gompper and G. E. Karniadakis, *Proc Natl Acad Sci U S A*, 2011, **108**, 11772–7.
44 J. F. Zhang, P. C. Johnson and A. S. Popel, *Phys. Bio.*, 2007, **4**, 285.
45 B. Dünweg and A. Ladd, *Adv. Polym. Sci.*, 2008, **221**, 89.
46 S. Succi, *The Lattice Boltzmann Equation for Fluid Dynamics and Beyond*, Oxford University Press, Oxford, 1st edn, 2001.
47 D. Wolf-Gladrow, *Lattice-Gas Cellular Automata and Lattice Boltzmann Models: An Introduction*, Springer, 1st edn, 2000.
48 J. R. Clausen and C. K. Aidun, *Phys. Fluids*, 2010, **22**, 123302.
49 M. Allen and D. Tildesley, *Computer Simulation of Liquids*, Clarendon Press, 1987.
50 P. Ahlrichs and B. Dünweg, *Int. J. Mod. Phys. C*, 1998, **9**, 1429.
51 C. K. Aidun and J. R. Clausen, *Annu. Rev. Fluid Mech.*, 2010, **42**, 439.
52 R. Adhikari, K. Stratford, M. Cates and A. Wagner, *Europhys. Lett.*, 2005, **71**, 473.
53 M. Widom, J. Lidmar and D. R. Nelson, *Phys. Rev. E*, 2007, **76**, 031911.
54 D. R. Nelson and L. Radzihovsky, *Phys Rev A*, 1992, **46**, 7474–7479.
55 P. Ahlrichs and B. Dünweg, *J. Chem. Phys.*, 1999, **111**, 8225.
56 A. Ladd, *J. Fluid. Mech.*, 1994, **271**, 285.
57 A. Ladd, *J. Fluid. Mech.*, 1994, **271**, 311.
58 H. Hasimoto, *J. Fluid Mech.*, 1959, **5**, 317.
59 A. Karnis, H. L. Goldsmith and S. G. Mason, *Canad. J. Chem. Eng.*, 1966, **44**, 181.
60 S. C. Hur, A. J. Mach and D. Di Carlo, *Biomicrofluidics*, 2011, **5**, 22206.
61 C. E. Chaffey, H. Brenner and S. G. Mason, *Rheol. Acta*, 1965, **4**, 56.
62 P. Olla, *J. Phys. II France*, 1997, **7**, 1533.
63 M. Abkarian and A. Viallat, *Biophys. J.*, 2005, **89**, 1055.

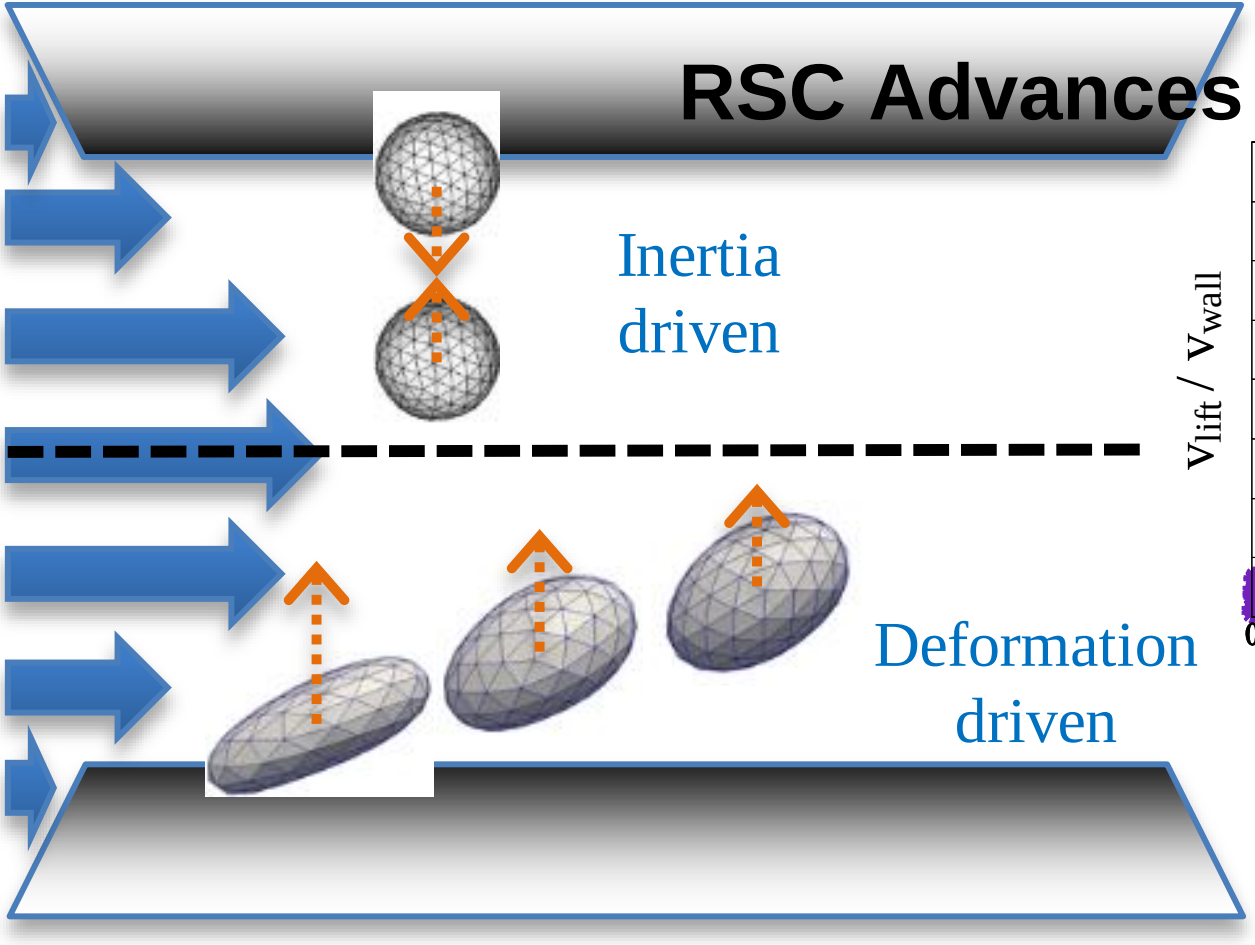

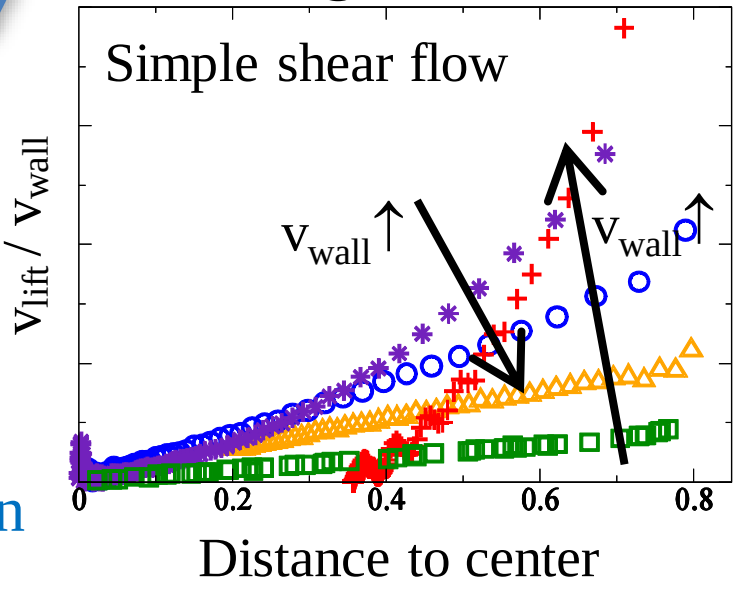

Nonlinear soft particle lift caused by inertia- and deformation-driven lateral migration, leading to migration-free zone in shear flow.